Received: 1 April 2021 | Revised: 3 January 2022 | Accepted: 13 January 2022

DOI: 10.1002/jev2.12193

RESEARCH ARTICLE

Transfer of photothermal nanoparticles using stem cell derived small extracellular vesicles for in vivo treatment of primary and multinodular tumours

María Sancho-Albero[1,2,3] | **Miguel Encinas-Giménez**[1,2,3] | **Victor Sebastián**[1,2,3] | **Estela Pérez**[4] | **Lluís Luján**[4,5] | **Jesús Santamaría**[1,2,3,6] | **Pilar Martin-Duque**[6,7]

[1] Instituto de Nanociencia y Materiales de Aragón (INMA), CSIC-Universidad de Zaragoza, Zaragoza, Spain

[2] Department of Chemical Engineering and Environmental Technologies, University of Zaragoza, Zaragoza, Spain

[3] Networking Research Centre on Bioengineering Biomaterials and Nanomedicine (CIBER-BBN), Madrid, Spain

[4] Department of Animal Pathology, University of Zaragoza, Zaragoza, Spain

[5] Instituto Universitario de Investigación Mixto Agroalimentario de Aragón (IA2), University of Zaragoza, Zaragoza, Spain

[6] Instituto Aragonés de Ciencias de la Salud /IIS Aragón, Zaragoza, Spain

[7] Fundación Araid, Zaragoza, Spain

Correspondence
Jesús Santamaría, Instituto de Nanociencia y Materiales de Aragón (INMA), CSIC-Universidad de Zaragoza, Zaragoza, Spain.
Email: jesus.santamaria@unizar.es
Pilar Martin-Duque, Instituto Aragonés de Ciencias de la Salud /IIS Aragón, Zaragoza, Spain.
Email: mariadelpilar.martin@unizar.es, mpmartind@gmail.com

Present address
María Sancho-Albero, Department of Molecular Biochemistry and Pharmacology, Instituto di Richerche Farmachologiche Mario Negri IRCCS 20156, Milano, Italy
Pilar Martin-Duque, Department of Surgery, University of Zaragoza Medical School, University of Zaragoza, Zaragoza, Spain

Abstract

The main current challenges in oncology are (1) avoiding systemic side effects in therapy, and (2) developing alternative treatment strategies for metastatic tumours. Nanomedicine was assumed to provide answers to these issues, but delivering enough therapeutic nanoparticles (NPs) to tumours still remains a huge challenge in nanomaterials-based treatments. Extracellular vesicles (EVs) play a key role in cell communication processes and can be combined with nanomaterials to improve their targeting capabilities. In this work, we leverage the ability of EVs derived from stem cells to reach tumour areas successfully, being used as delivery vehicles for nanoparticles acting as hyperthermia agents. Once small extracellular vesicles (sEVs) loaded with NIR-sensitive hollow gold NPs reached primary subcutaneous solid tumours, they were irradiated with a NIR laser and almost complete tumour remission was obtained. More interestingly, those sEV vehicles were also able to reach multinodular areas similar to those on advanced metastatic phases, eradicating most tumour growth regions in multiple cancerous nodules located in the pancreas region.

KEYWORDS

Extracellular vesicles, optical hyperthermia, gold nanoparticles, multinodular cancer and NIR laser

1 | INTRODUCTION

Cancer remains as one of the leading causes of morbidity and mortality worldwide, with 18.1 million of newly diagnosed cases in 2018. Those numbers are projected to continue rising, with an estimated 29.5 million of new cases in 2040 according to the

International Agency for Research on Cancer (IARC- International Agency for Research on Cancer 2020). In addition to surgery, chemotherapy and radiotherapy that are the standard therapeutic approaches for cancer treatment in the clinic, other strategies such as immunotherapy, hormonal or viral therapies are emerging as alternative treatments with lower side effects (Jhawar et al., 2017, Prat and Baselga, 2008). Nevertheless, more effective methods are still necessary to allow therapies to reach tumoral areas efficiently and selectively, in order to increase antitumoral activity while decreasing their side effects in healthy organs and tissues.

Among the novel therapies proposed toward that objective, near-infrared (NIR) hyperthermia uses NIR-absorbing NPs (e.g., hollow gold nanoparticles (HGNs)) (Jhawar et al., 2017, Rastinehad et al., 2019), which typically exploit the phenomenon of surface plasmon resonance to transform the energy of the incident light into heat. The NIR region of the spectrum is preferred because the absorption and the scattering of light are minimized thanks to the reduced absorption by water and by chromophores (i.e., haemoglobin and melanin). When the NIR-absorbing NPs are inside a tumour, the increase in temperature produced by light irradiation causes cell death by apoptosis or necrosis leading to the ablation of the tumour (Rastinehad et al., 2019, Sharma et al., 2019). Compared to magnetic hyperthermia, NIR-based hyperthermia is safer because the increase in temperature is limited to the region illuminated by the NIR laser beam. However, to achieve tumour death, a sufficient number of NPs needs to be delivered selectively to the tumour, a challenging task since the efficiency of nanoparticle delivery to tumours is currently around 1% (Wilhelm et al., 2016).

Small extracellular vesicles (sEVs) are nanosized extracellular vesicles (from 50 to 150 nm of diameter) of endocytic nature secreted by almost every type of cell in the human body (Colombo et al., 2014). They present a double lipid membrane that surrounds sEVs cargo (i.e., proteins, lipids and nucleic acids). They have high stability in physiological conditions, low immunogenicity, prolonged circulation time and, more importantly, targeting specificity toward their parental and related lineage cells (Khongkow et al., 2019, Sancho-Albero et al., 2019, Sancho-Albero et al., 2019, Yong et al., 2019). sEVs are considered key players in intercellular communication and in modulating interactions between cells and their environment (Kahlert and Kalluri, 2013, Lachenal et al., 2011, Shahabipour et al., 2017). Given these characteristics, sEVs have raised great interest as potential vectors capable of selectively delivering NPs with higher efficiency to tumours. Thus, magnetic NPs have been encapsulated within sEVs for tumour imaging (based on MRI) and treatment (by magnetic hyperthermia) (Hu et al., 2015, Hood et al., 2014, Zhuang et al., 2020). A few works have also combined gold NPs with sEVs for cancer theragnosis (Alhasan et al., 2009, Betzer et al., 2017, Lara et al., 2020, Roma-Rodrigues et al., 2017). However, there are no studies using sEVs loaded with gold NPs for cancer treatment by optical hyperthermia. This is mainly due to the intrinsic difficulty of encapsulating NIR-responsive NPs (HGNs are typically 40–60 nm in size) within sEVs without disrupting their membranes, as this would compromise their selective targeting capabilities.

In a previous work we demonstrated that one way to achieve this goal is to leverage the sEVs biogenesis pathway, by incubating the target cells with HGNs and harvesting the loaded sEVs with their intact membranes (Sancho-Albero et al., 2019). Encouraged by these results, here we explore the possibility of using stem cells derived sEVs-HGN hybrids as in vivo therapeutic tools in animal models. Also, unlike most of the published studies that target xenograft primary tumours, herein we have further challenged the selective delivery capabilities of sEVs by using them also to treat a multinodular intraperitoneal model in an effort to address a scenario that is more similar to finding and fighting metastatic tumours.

2 | MATERIALS AND METHODS

2.1 | PEG-HGNs-sEVs^{hpMSCs} purification and characterization

sEVs parental cells, thus hpMSCs, were obtained from Cellular engineering Technologies (CET (Coraville, IA, USA) and were grown in Dulbecco's modified Eagle's medium (DMEM, Biowest, France) supplemented with 5 μg ml^{-1} of FGF-2 growth factor (PeproTech, USA), with 10% of foetal bovine serum (FBS, GIBCO, USA), 1% penicillin/streptomycin and 1% amphotericin (Biowest, France) and maintained at 37 °C in a 5% CO2-humidified atmosphere under hypoxic conditions (3% O2). To obtain the culture media free of sEVs (Ultracen media), they were depleted from serum by ultracentrifugation at 100,000 g for 8 h at 4 °C.

sEVs from hpMSCs were isolated following an ultracentrifugation protocol previously reported by our group (Figure S1) (Sancho-Albero et al., 2019, Sancho-Albero et al., 2019). Briefly, cells were seeded in cell culture dishes until they reached 80% of confluence. After that, they were washed and the cell culture media was replaced by Ultracen media free of sEVs and cells were maintained during 48 h. For the purification of the PEG-HGNs-sEVs^{hpMSCs} cells were treated with PEG-HGNs during 24 h at 0.1 mg/ml. Then, they were also washed with PBS in order to eliminate the non internalized nanoparticles and they were maintained during 48 h with Ultracen media as control cells. Supernatants from both control and treated cells were collected and were centrifuged for 20 min at 2000 g at 4 °C. For discarding the microvesicles, samples were centrifuged during 30 min at 10,000 g and at 4 °C. To finally isolate sEVs, samples were ultracentrifuged twice for 2 h at 100,000 g and at 4 °C. The final precipitates were suspended in PBS and a Pierce BCA protein assay (Thermo Fisher Scientific, USA) was performed in order to estimate the protein content in the sEVs sample following the instructions provided by the manufacturer.

Then, both sEVs^{hpMSCs} and PEG-HGNs-sEVs^{hpMSCs} were thoroughly characterized. Western Blot analysis was performed in order to analyze the content-specific sEVs surface proteins. We have also already published their biological characterization including: cytotoxicity assays, internalization evaluation both by confocal microscopy and by MP-AES, and their in vitro photothermal therapy properties in both mono- and cocultures (Sancho-Albero et al., 2019, Sancho-Albero et al., 2019). Western Blot analysis was performed in order to analyse the content-specific sEVs surface proteins. In summary, 15 μg of sEVs (obtained by BCA and expressed as total protein amount) were suspended in Laemmli buffer and was incubated at 95 °C during 3 min. Proteins were subsequently separated in a 10% SDS-PAGE gel at 20 mV during 2–3 h and transferred to a nitrocellulose membrane at 4 °C during 2 h (100 mV). Blots were blocked during 1 h with TTBS buffer containing 5% of BSA at room temperature. Finally, they were incubated with the sEVs antibodies: CD9 (EPR2949, cat n:ab92726, 1:2000, Abcam), CD63 (Ts63, cat no. 10628D, 1:1000, BD Biosciences), CD81 (B-11, cat no. sc-166029,1:500, Santa Cruz Biotechnology), TSG101 (51/TSG101, cat no. 612697, 1:1000, BD Biosciences) and α-tubulin (cat no. 2144, 1:1000, Cell Signalling Technologies). Membranes were washed three times with TTBS followed by incubation of the secondary antibody (goat-anti-mouse IgG, HRP cat no. 1030-05 Southern Biotech, and Goat-anti-rabbit IgGHRP, cat no. A0545 Sigma Aldrich). Before being imaged by chemiluminescence, they were washed three times again. NTA analysis (Nanosight NS200, Malvern Panalytical) was performed in order to determine the diameter and the concentration (particles per ml) of both empty and PEG-HGN loaded sEVs. sEVs were also characterized by TEM (T20-FEI Tecnai transmission electron microscopy) operated at 200 kV and using phosphotungstic acid (3%) as negative contrast agent to stain the sEVs.

The PEG-HGNs-sEVs^{hpMSCs} were labeled with the Cell Claret Far Red (ex/em 655/675) Fluorescent Cell Linker (Sigma Aldrich). To do that, sEVs pellet was resuspended in 1 ml of PBS and 4 μl of the fluorescent linker were also diluted in 4 μl of PBS. Then, the fluorescence probe was added to the sEVs sample and they were kept in contact during 5 min. After that time, 1 ml of FBS was added to the mixture in order to stop the reaction. Finally, the volume was completed until 33 ml with PBS and sEVs were ultracentrifuged at 100,000 g during 2 h to discard the nonbound (free) fluorescent linker.

In order to evaluate if the fluorescent signal of the sEVs was stable, the signal of the sEVs was analysed 24 h, 48 h, 72 h and 1 week after of their labelling. To do that, sEVs were ultracentrifuged at those different time-points and the signal in the sEVs pellet and supernatant was measured by using a Multi–Modal Lector Synergy HTX (Bioteck, Agilent) at 630 nm (absorbance). Before performing the in vivo experiments, the PEG-HGNs-sEVs^{hpMSCs} behaviour as efficient transductors of light into heat was determined by measuring the UV-VIS absorption spectra and monitoring the temperature increase during 14 min after their exposition to a NIR laser as mentioned in the supplementary information.

2.2 | Animal and tumour models optimization

All the procedures of this study were performed under the Project Licenses PI 28/19 and PI04/19 approved by the Ethic Committee for Animal Experiments from the University of Zaragoza (*Comisión Ética Asesora para la Experimentación Animal de la Universidad de Zaragoza*). Mice were fed ad libitum and their care and maintenance under specific pathogen-free conditions were performed accordingly with the Spanish Policy for Animal Protection RD53/2013, which meets the European Union Directive 2010/63 on the protection of animals destined to experimental and other scientific purposes.

For these experiments 6- to 8-week-old female BALB/c nu/nu mice (Envigo) were employed. All the animals were maintained under quarantine during 7 days as soon as they arrived to the animal facilities and before starting the experiments. For the xenograft model, animals received a subcutaneous injection of 3×10^6 HeLa cells suspended in 200 μl of DPBS. In the multinodular model, 8×10^5 SKOV_Luc cells (stable infected with the luciferase reporter gene kindly given by Dr. Antonio de la Vieja from *Instituto de Salud Carlos III*) were intraperitoneally injected to the mice. In order to evaluate potential weight loss during the experiments, mice were weighed daily. In the xenograft model, tumours were measured with a caliper and in the multinodular model, the number of tumours as well as their size were evaluated under IVIS Lumina imaging due to the luminescence of the implanted SKOV_Luc cells.

Two different and independent experiments were carried out in order to evaluate the biodistribution and the toxicity of the PEG-HGNs-sEVs^{hpMSCs} and to assess the efficiency of the photothermal therapy. The manipulation of the animals in the procedures was performed under sterile conditions in a hood.

2.3 | In vivo photothermal studies

Before attempting the photothermal studies, the laser irradiation (time and power) and, in the case of the multinodular model, the introduction of the laser probe, were optimized in a previous pilot study using ex vivo experiments. The spleen, liver and pancreas from waste mice were collected and were irradiated with the laser with 1.5; 2 and 2.5 W of power in order to verify the increase on temperature when enhancing the power. To do that, 1.71×10^{10} particlesof PEG-HGNs-sEVs^{hpMSCs} (corresponding with 100μg expressed in total protein amount) were inoculated within the organ immediately before the laser application with

a needle and a syringe. Then, the temperature was measured 0, 2.5 and 5 min after laser application with a thermocouple and a Testo 925 channel Thermometer.

In the in vivo photothermal studies, the animals were divided in four groups: group 1 control without sEVs and without laser irradiation; group 2 control without sEVs and with laser irradiation; group 3 control with sEVs without laser irradiation; and group 4 with sEVs and with laser irradiation. During the irradiation, animals were initially anesthetized with 5% isoflurane and maintained with 1−2% isoflurane (1 L/min oxygen flow). They were irradiated within a sterile hood while resting on an electric pad to avoid hypothermia when animals were exposed to anaesthesia.

In the case of the xenograft model, 15 days after the tumour implantation, 1.71×10^{10} particles of PEG-HGNs-sEVs^{hpMSCs} were intravenously administered to mice from groups 3 and 4. Then, 48 h later, groups 2 and 4 were irradiated with a NIR-laser (808 nm) at a power of 2 W during 5 min. The temperature was monitored at different time points during the irradiation (0, 2.5 and 5 min) with a temperature sensor. Tumour size was periodically evaluated by using a caliper up to 1 week after irradiation. Aloe Vera VET was cutaneously applied to the tumours of animals treated with the laser in order to promote the healing of the wound caused by the laser (in the case of group 4). One week after the first sEVs administration, PEG-HGNs-sEVs^{hpMSCs} were again intravenously administered in the mice tail and 48 h after their administration, they were irradiated with the laser in the same conditions of the first irradiation. Tumour size was assessed using a caliper during the following week and Aloe Vera VET was also cutaneously applied to the tumours. Tumour size was measured with a caliper during the next 27 days after tumour implantation.

In order to evaluate the potential application of this method in a multinodular model, 800,000 SKOV_Luc cells were intraperitoneally administered to the mice and were allowed to grow during 10 days. Mice were divided in the same four groups used with the xenograft model. After that, 1.71×10^{10} particles of PEG-HGNs-sEVs^{hpMSCs} were intravenously administered in the mice tail of animals from group 3 and 4. Then, 72 h later, animals were irradiated with a NIR-laser (808 nm) with a power of 1.5 W during 5 min (groups 2 and 4). The temperature was monitored at different time points during the irradiation (0, 2.5 and 5 min). In this particular model, as the cancerous nodules were within the peritoneum, a surgery was needed. The Figure S2 shows an illustration of both optic fibres employed for both models. In the xenograft Model a cylindrical collimator of 300 μm was used in order to obtain a homogenous and parallel beam concentrated in the tumour area. In the multinodular Model, a cylindrical radially emitting fibre was used. In order to be as less invasive as possible, a cylindrical light diffuser used for intraperitoneal phototherapy was thin (0,98 mm) and very flexible (Medlight S.A.). For the surgical procedure, mice were initially anesthetized with 5% isoflurane and maintained with 1–2% isoflurane (1L/min oxygen flow). Then, a small incision was performed in the mice skin iat the flank of the spleen and the pancreas with surgery micro scissors. Then, the same incision was carried out in the peritoneum and the laser probe was intraperitoneally introduced. Laser was applied during 5 min and the temperature was registered at different time points during the irradiation (0, 2.5 and 5 min) with a temperature sensor (Testo 925 channel Thermometer). Then, the incision was sutured and buprenorphine (2.5 mg/kg body weight) was subcutaneously administered for pain relief (daily until 48 h postsurgery). After 1 week, a secondary laser application cycle was applied to the mice using the same conditions. Tumour size and the number of nodules were measured by luminescence (by IVIS Lumina) during 24 h from the tumour implantation. The in vivo photothermal procedure in both tumour model is illustrated in the Figure 1.

2.4 | Histopathological studies

Euthanasia of the animals was performed by CO_2 inhalation. Then, tumour, kidneys, liver, lungs, spleen and pancreas were collected. Moreover, the skin of the tumours and the skin in the area of the surgery of the photothermal studies were removed and processed.

In the biodistribution experiments from both tumoral models, samples were fixed in 4% paraformaldehyde (Alfa Aesar) for 24 h, followed by cold 70% ethanol. Tissue samples were then embedded in paraffin and three micrometre sections were stained with haematoxylin and eosin (HE). In order to evaluate the presence of the fluorescence sEVs within the tumours and the pancreas containing the multiple nodules, an immunofluorescence analysis by confocal microscopy was carried out (Zeiss LSM 880). To do that, samples were frozen with isopentane cooled by liquid nitrogen and cryosectioned at five micrometres. Slices were assembled in a slide with FluoromontG and DAPI (ex/em 364/454) for visualization. In the confocal microscope analysis, a multialignment of 10×10 images Z-stack images with the 20x objective were performed in order to visualized the whole tissue. PEG-HGNs-sEVs^{hpMSCs} were visualized due to their fluorescence from the Claret probe (ex/em 655/675).

In the photothermal studies, three micrometre sections of the organs were stained with HE as previously mentioned. In order to assess tumour proliferation and remission, an immunohistochemical evaluation was performed by using a human Ki-67 antibody (Agilent). The automated immunostaining platform Autostainer Link (Dako) was employed. Sections (4–5 μm) were dewaxed and rehydrated with dH_2O and antigen retrieval was performed by heat at pH = 7 during 20 min. Samples were incubated with primary Ki-67 antihuman antibody during 20 min, followed by the visualization system conjugated with horseradish peroxidase (Flex/HRP system, Agilent) using haematoxylin staining as contrast. Finally, sections were dehydrated and mounted. Samples were visualized under a conventional microscopy (Widefield inverted microscope Olympus IX81). Ki-67 protein expression was

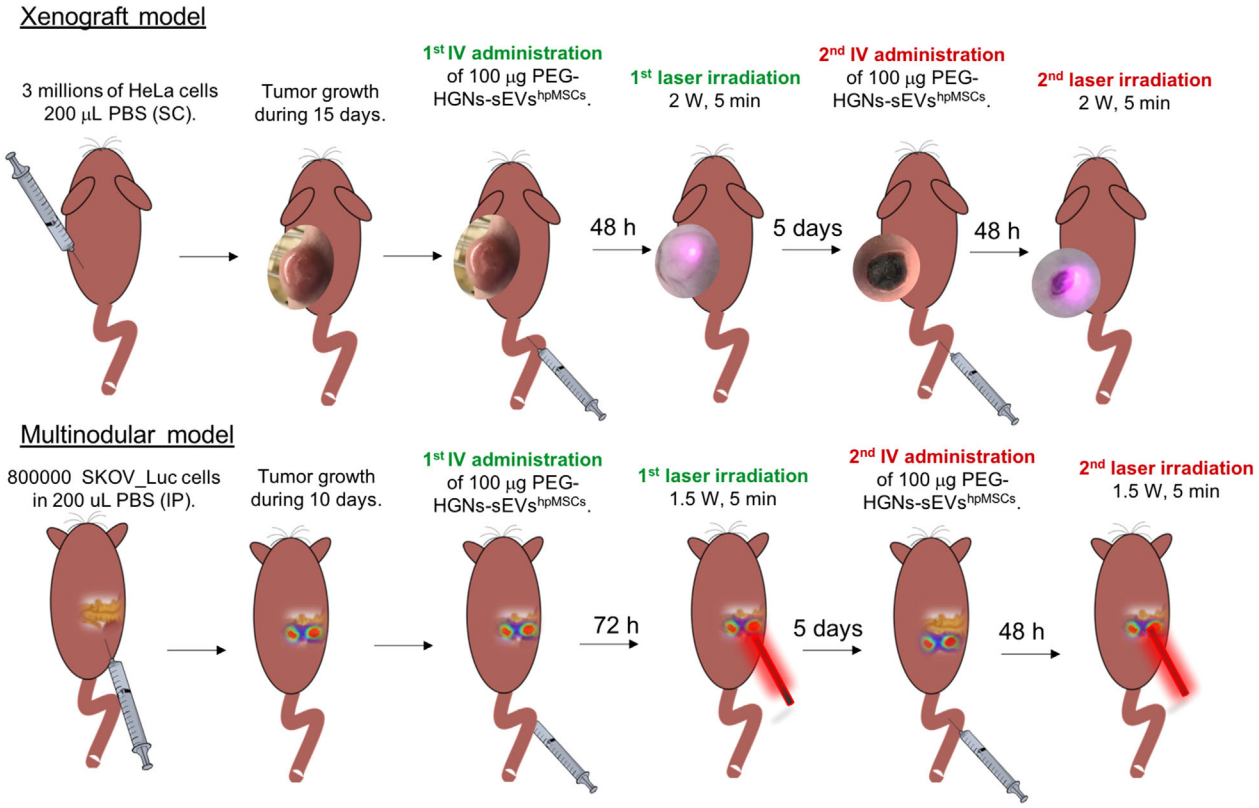

FIGURE 1 Scheme with the experimental sequence followed for the photothermal treatment mediated by the PEG-HGNs-sEVs^{hpMSCs} of the tumours in the xenograft and multinodular model

assessed in all mice groups by counting positive and negative cells in three acquisition images from all animals from each group using ImageJ software to obtain the percentage of positive cells.

2.5 | Statistical analysis

All the results are expressed as mean ± SD. Statistical analysis of the data and the significant differences among the means were analysed by two-way analysis of variance (ANOVA) for multiple comparisons by Dunnett's multiple comparisons test (GraphPad Software). Statistically significant differences were expressed as follows: $*p < 0.05$; $**p < 0.01$; $***p < 0.0001$ y $****p < 0.00001$.

3 | RESULTS

3.1 | HGN encapsulation in sEVs

Following the procedures of our previous works, HGNs were incubated with mesenchymal stem cells (hpMSCs) and the HGN-loaded sEVs were collected by centrifugation. Figure 2(a) shows the appearance of the HGNs as prepared and after coating with a polyethylene glycol (PEG) layer. Their spectrum shows a strong absorbance peak in the NIR region and, as a consequence, a rapid heating under irradiation by a 808 nm laser (Figure 2b and Figure 2c). After incubation, the NPs were taken by the MSCs and expelled inside sEVs. Figure 2(d) shows that the sEVs were often loaded with more than one nanoparticle, a useful characteristic to increase heat generation upon illumination with NIR light. From TEM images by counting approximately 200 sEVs, we observed that more than 50% of the sEVs were loaded with at least one HGN. In particular, 53.6% of the sEVs were loaded with the photothermal nanoparticles. These results are in agreement with our previous studies, where we have demonstrated that large proportion (almost 50%) of the sEVs produced by cells after incubating them with PEG-HGNs were loaded with at least one nanoparticle (Sancho-Albero et al., 2019). Among the loaded sEVs, 47%, 28% and 25% of them were loaded with one, two or three or more nanoparticles, respectively. With this procedure, the internalization yield is significantly higher compared with

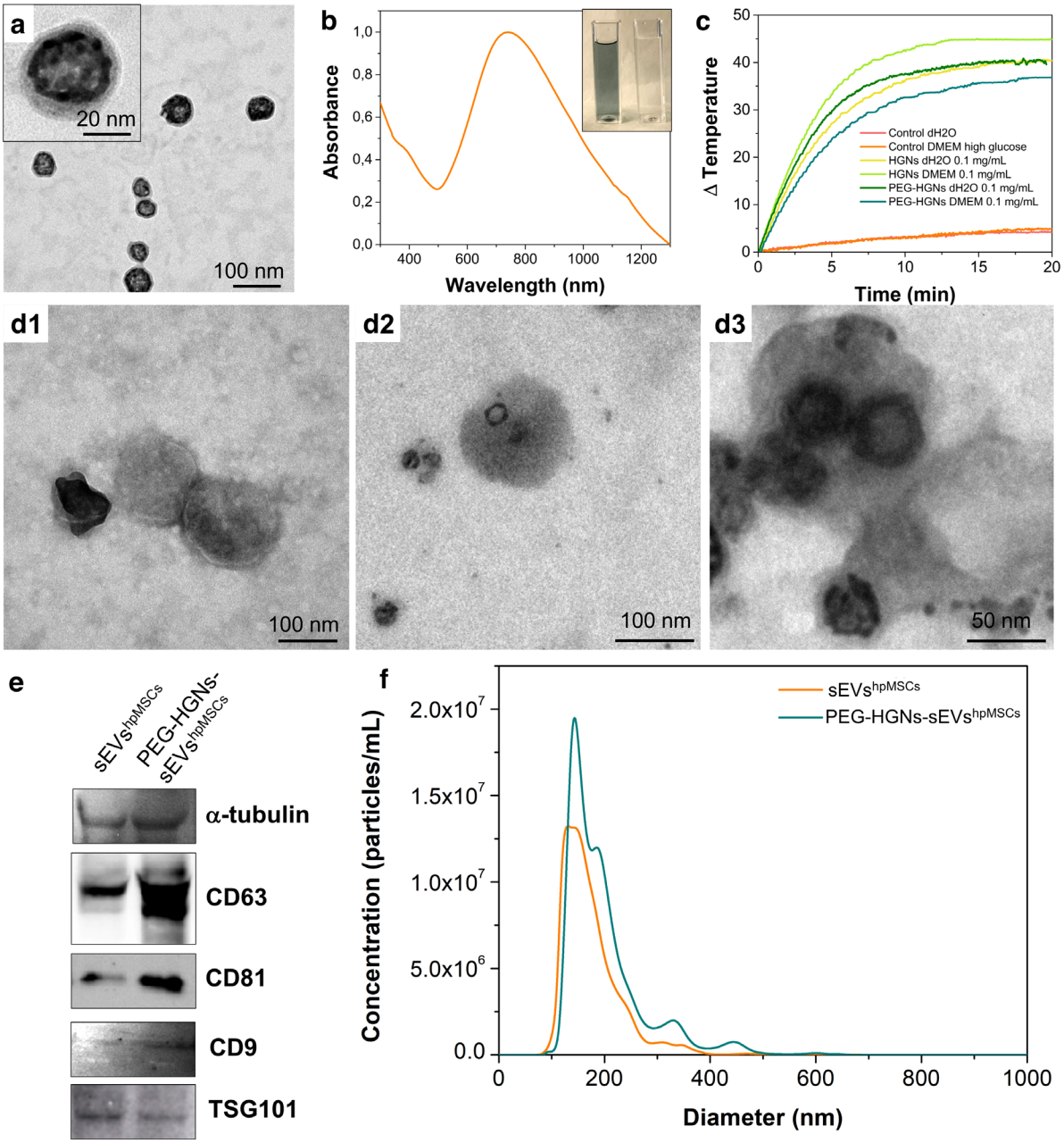

FIGURE 2 Characterization of pegylated HGNs (PEG-HGNs) and PEG-HGNs-sEVs^{hpMSCs}. (a) TEM images of PEG-HGNs exhibiting a PEG shell. (b) UV-VIS absorption spectra of PEG-HGNs with a maximum peak in the NIR region. (c) Heating efficiency of NPs in DMEM and water as solvents under 808 nm wavelength laser irradiation. The increase of the temperature at constant laser power of the particles at the subcytotoxic dose is represented. (d) TEM images of control (d1) and PEG-HGNs-sEVs^{hpMSCs} (d2-d3). (e) Western Blot against α-tubulin, CD63, CD81, CD9 and TSG101 proteins in both control and loaded sEVs. (f) Nanosight analysis of sEVs^{hpMSCs} and PEG-HGNs-sEvs^{hpMSCs}

exogenous physicochemical methods, which result not only in low loading yields but also can lead to irreversible damage, likely compromising sEVs integrity.

We have also already published their biological characterization including: cytotoxicity assays, internalization evaluation both by confocal microscopy and by MP-AES and their in vitro photothermal therapy properties in both mono- and co-cultures [9,22]. To verify their sEVs nature and to corroborate that the presence of the particles did not interfere with the expression of specific proteins, western blot against CD9, CD63, CD81 and TSG101 (sEVs proteins) as well as against α-tubulin as housekeeping protein was carried out (Figure 2e). As well, NTA analysis included in Figure 2(f) clearly indicates that the presence of the nanoparticles within the sEVs do not affect their diameter and morphology (both sEVs^{hpMSCs} and PEG-HGNs-sEVs^{hpMSCs} exhibited a diameter of 173.8 ± 54.6 nm and 196.7 ± 75.5 nm, respectively). Protein amount obtained by the BCA assay were 878.8 μg/ml (15.02 x10^{10} particles/mL) and 1088.6 μg/ml (18.61 x10^{10} particles/mL) for sEVs^{hpMSCs} and PEG-HGNs^{hpMSCs}, respectively. Analysing the sEVs

concentration measured by NTA and the expression of sEVs proteins assessed by WB, higher amounts of sEVs were secreted from cells treated with NPs compared to the amounts measured for control samples (untreated cells).

Figure S3(A) shows the UV-VIS spectrum of PEG-HGNs-sEVs^{hpMSCs} exhibiting a maximum absorption peak around 690 nm, slightly shifted from the 808 nm maximum peak of PEG-HGNs. This change could be attributed to the interactions between the solute and solvent, as well as to the fact that nanoparticles were encapsulated within sEVs rather than naked, which can affect the solute's absorption spectra by modifying the electronic structure and the dipolar moment of the solute. Nevertheless, Figure S3(B) corroborates a rapid heating increase of temperature by irradiating PEG-HGNs-sEVs^{hpMSCs} with the NIR light laser compared to empty exosomes (control).

3.2 | In vivo biodistribution, xenograft model

The biodistribution of the sEVs derived from hpMSCs loaded with pegylated HGNs (PEG-HGNs-sEVs^{hpMSCs}) administered in in vivo experiments was firstly assessed *ex vivo* by IVIS in both tumoral models (Figure S4). This was done to obtain a higher sensitivity by examining directly the organs concerned rather than the whole animal, and also to avoid artifacts due to the fact that the xenograft tumour grows subcutaneously rather than internally and therefore it may give a disproportionately high fluorescence signal compared to inner organs under whole body evaluation. Figure 3(a) shows sEVs bioaccumulation quantified

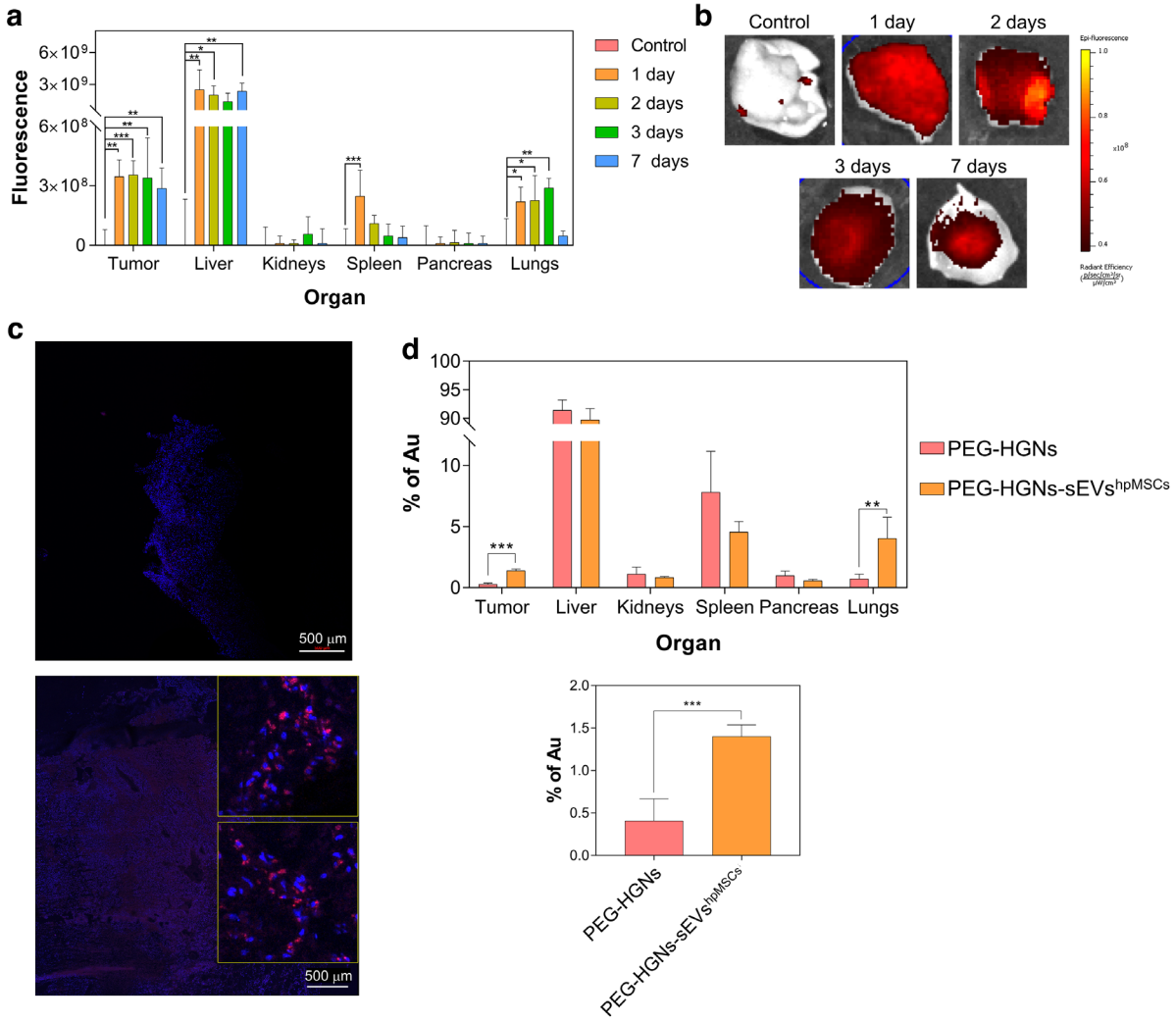

FIGURE 3 Biodistribution of PEG-HGNs-sEVs^{hpMSCs} in xenograft murine model. (a) in vivo biodistribution of the PEG-HGNs-sEVs^{hpMSCs} in different organs. (b) *Ex vivo* fluorescence images of the xenograft tumours after 24, 48, 72 h and 1 week of intravenous administration of the PEG-HGNs-sEVs^{hpMSCs}. (c) Confocal microscopy images of immunofluorescence labeling of tumour tissues of untreated mice (up) and mice treated with PEG-HGNs-sEVs^{hpMSCs} after 2 days (down). The nuclei of the cancerous cells were marked with DAPI and appear in blue, while the fluorescent sEVs are observed as red aggregates in the cytoplasm of these cells. (d) ICP-MS analysis of gold in organs extracted from mice after PEG-HGNs-sEVs^{hpMSCs} and free PEG-HGNs (up) intravenous administration, detail of Au content present in the tumour detected by ICP-MS (bottom). *$p < 0.05$; **p < 0.01; ***p < 0.0001

from analysis of fluorescence in the xenograft model. It can be observed that liver, lungs and tumour were the main sEVs accumulation sites. The statistical analysis of these results was studied organ by organ, comparing the fluorescence level of the organs from mice treated with the PEG-HGNs-sEVs^{hpMSCs} with the organs from the control mice, taking into account that all control organs present a baseline fluorescence signal. It is important to indicate that negligible fluorescence was observed in kidneys or pancreas for any of the time points assessed, suggesting that sEVs accumulation in these organs was minimal. In the lungs, a growing accumulation of sEVs was observed during the first 72 h. However, it is interesting to note that after 1 week the sEVs signal disappeared.

From the fluorescence results of the tumour, it can be concluded that the maximum accumulation of PEG-HGNs^{hpMSCs} occurs after 48 h, although there is little difference between fluorescence levels between 24 and 72 h (Figure 3b). The immunofluorescence *post mortem* analysis of the tumours again corroborates the high concentration of PEG-HGNs-EVs^{hpMSCs} in the tumour after 48 h as well as its distribution throughout the tumour mass compared with untreated mice (Figure 3c). sEVs are still observed after 72 h and 1 week (Figure S5), although their concentration decreased compared with the samples of 48 h, in broad agreement with the biodistribution data of Figure 3(a).

As a more accurate alternative to fluorescence measurements, the biodistribution of PEG-HGNs-sEVs^{hpMSCs} was also estimated by measuring the amount of gold in the different organs by ICP-MS after organ digestion. In agreement with the fluorescence measurements, a large majority of Au was localized in the liver, and 1,5% of the gold was found in the tumour (Figure 3d). Specifically, the percentages of Au in each organ after 48 h of administration were as follows: liver (89.74 ± 1.99%), spleen (4.56 ± 0.85%), lungs (3.44 ± 1.84%), tumour (1.40 ± 0.13%), kidneys (0.84 ± 0.07%) and pancreas (0.58 ± 0.10%). While these results are less encouraging than the fluorescence results of Figure 3(a), they still represent a very significant improvement compared to enhanced permeability and retention (EPR)-based accumulation. When the experiment was repeated injecting the free PEG-HGNs (rather than encapsulated in the sEVs), the distribution of gold was as follows: liver (91.50 ± 0.34%), spleen (7.03 ± 4.36%), kidneys (1.11 ± 0.62%), lungs (1.01 ± 0.86%), pancreas (0.96 ± 0.39%) and tumour (0.4 ± 0.29%). These results indicate that encapsulation of the particles within the sEVs^{hpMSCs} was effective in targeting tumoral areas, where accumulation was around four times higher than that obtained by EPR effect alone. In fact, for particles encapsulated within sEVS, the tumour was the fourth organ with a higher amount of gold after liver, spleen and lungs. On the contrary, when the particles were freely administered, the lowest percentage of gold was found in the tumour.

The histopathological analysis carried out in the H&E stained sections of the animals treated with the PEG-HGNs-sEVs^{hpMSCs} did not reveal cellular morphological alterations that could be attributed to the accumulation of the sEVs in any of the tissues studied, when compared to control mice. Figure S6 includes representative H&E images of the tumour mass and organs such as liver, spleen, pancreas, kidneys and lungs from control mice and from sEVs-treated mice at 48 h and 1 week after treatment.

3.3 | In vivo biodistribution, multinodular model

The biodistribution of PEG-HGNs-sEVs^{hpMSCs} in the multinodular model, was again studied by IVIS fluorescence measurements. Multiple cancerous nodules were observed mainly in the pancreas (although some animals presented also some tumoral areas in the spleen). As in the xenograft model, analysis of the fluorescence in the different organs indicated that most of the PEG-HGNs-sEVs^{hpMSCs} accumulated in the liver and in the lungs at any time of the study (Figure 4a). Also, as in the xenograft model, the number of sEVs in the lungs was initially higher increasing over the first few days, then the vesicles tend to disseminate and disappear from this organ. In the pancreas (containing most of the tumour nodules) a statistically significant maximum accumulation of the sEVs was observed after 72 h of their IV injection. Comparing those results with the same experiment performed in the xenograft model (where no fluorescence signal was observed in the pancreas at none of the time points of the study), it can be concluded that the enhanced migration of sEVs to the pancreas only occurs when tumoral nodules are present, sEVs likely accumulating in tumour tissue and not in pancreatic parenchyma. Moreover, an accumulation of sEVs was also observed in the spleen, (that also presented tumoral areas mainly in the junction of the splenopancreatic region) confirming again that the preferential tropism of sEVs to tumours and areas of inflammation occurs not only in a xenograft model (primary solid tumour) but also in a multinodular cancerous model (simulating a metastasis). Figure 4(b) shows *ex vivo* bioluminescence and fluorescence images of pancreas with multinodular tumours after 1, 2, 3 and 7 days where a clear accumulation of PEG-HGNs-sEVs^{hpMSCs} can be observed. The bioluminescence signal indicates that tumour nodules were present in the same region at those times.

The immunofluorescence analysis performed by confocal microscopy in the pancreatic tissue (where the majority of tumour nodules were located) is shown in Figure 4(c). As in the xenograft model, these acquisitions confirm that the maximum accumulation of the PEG-HGNs-sEVs^{hpMSCs} in the pancreas occurs after 72 h of their administration, also in agreement with the results in Figure 4(a). In control (untreated) mice no fluorescence signal was observed. On the other hand, after 24 and 48 h, the accumulation of PEG-HGNs-sEVs^{hpMSCs} was too weak to be observed by confocal microscopy (Figure S7). After 1 week,

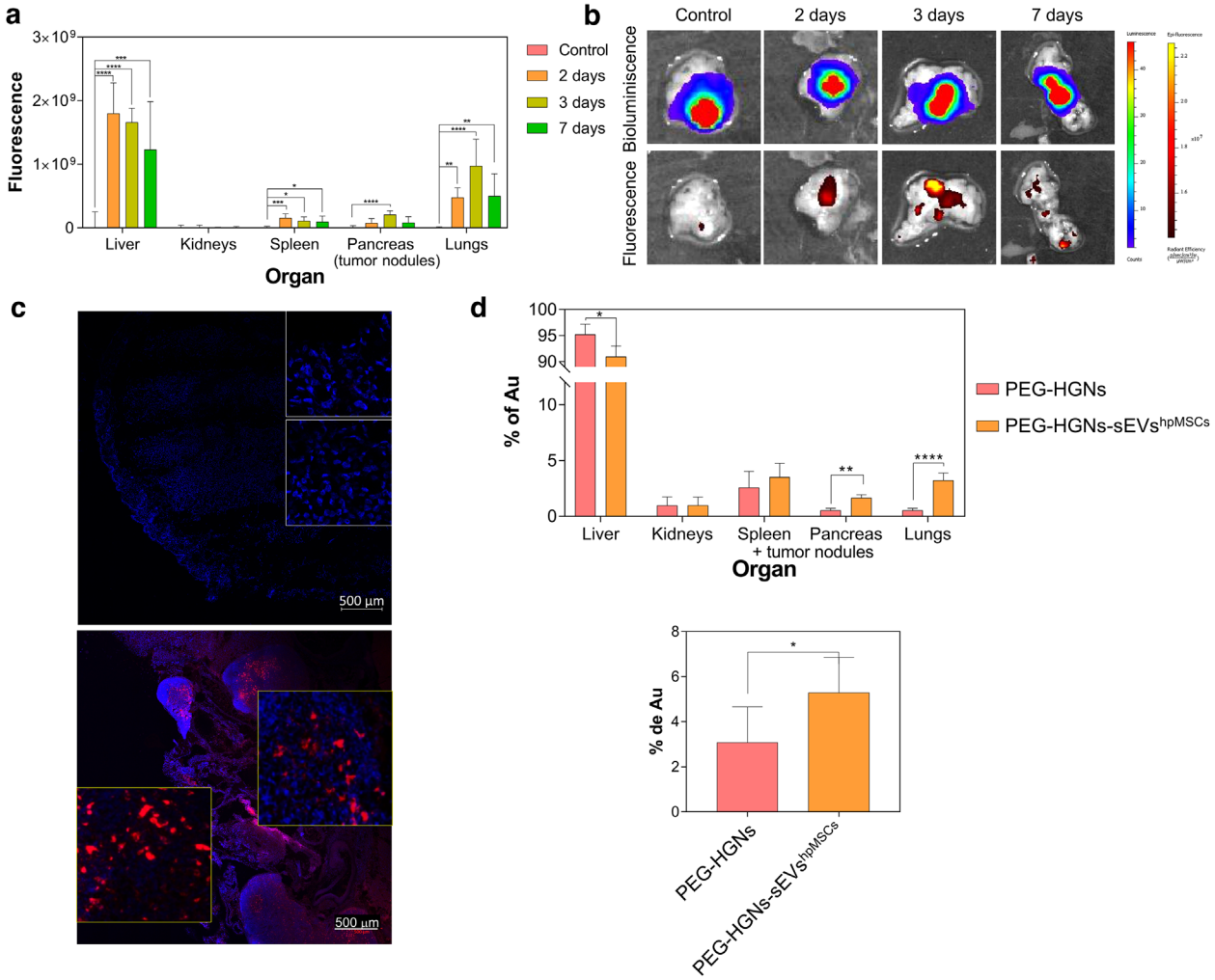

FIGURE 4 Biodistribution of PEG-HGNs-sEVs^{hpMSCs} in multinodular murine model. (a) in vivo biodistribution of the PEG-HGNs-sEVs^{hpMSCs} in mice with a multinodular model from fluorescence measurements (b) Visualization of the multinodular cancerous regions in the pancreas by bioluminescence and the PEG-HGNs-sEVs^{hpMSCs} by fluorescence after 24, 48, 72 h and 1 week after their intravenous administration. (c) Confocal microscopy images of immunofluorescence labeling of pancreatic tissue in of untreated mice (up) and in mice treated with PEG-HGNs-sEVs^{hpMSCs} (down) and sacrificed after 72 h, containing the multinodular model. (d) ICP-MS analysis of gold in organs extracted from mice after PEG-HGNs-sEVs^{hpMSCs} and free PEG-HGNs (up) intravenous administration, detail of Au content present in the tumoral areas located in the pancreas and spleen and detected by ICP-MS (bottom). *$p < 0.05$; **$p < 0.01$; ***$p < 0.0001$; ****$p < 0.00001$

there was still an amount of the sEVs retained in the organ, potentially still capable to exert a therapeutic effect. However, this concentration was significantly lower than the concentration at the maximum accumulation time point (72 h).

Finally, the quantification of Au in the different organs after 72 h of the administration of the PEG-HGNs-sEVs^{hpMSCs} was carried out by ICP-MS (Figure 4d). These results demonstrated that although most of the gold was still localized in the liver, more than the 5% of the injected PEG-HGNs-sEVs^{hpMSCs} accumulated in the tumoral areas (located mainly at pancreas and spleen). More specifically, the percentage of Au in the organs was: liver (90.82 ± 2.08%), spleen with tumours (3.48 ± 1.24%), lungs (3.19 ± 0.65%), pancreas with the tumours (1.65 ± 0.28%) and the kidneys (0.98 ± 0.72%). This biodistribution is in sharp contrast with that obtained when free PEG-HGNs were administered: liver (95.21 ± 1.99%), spleen with tumours (2.55 ± 1.46%), kidneys (0.96 ± 0.75%), pancreas with the cancerous areas (0.74 ± 0.28%) and lungs (0.52 ± 0.18%). Comparing both biodistributions assays, it can be concluded that when PEG-HGNs are encapsulated within sEVs a strong increase in selectivity toward tumours occurs, enhancing the amount of gold delivered to target areas, while concomitantly the amount of gold captured in the liver decreases.

The H&E histopathological analysis of mice with the multinodular model did not revealed relevant histopathologic changes in any of the organs analysed that could be attributed to the accumulation of the PEG-HGNs-sEVs^{hpMSCs}. Figure S8 includes images of the H&E analysis of the different organs after 72 h and 1 week of the sEVs injection as well as of a control mice group (untreated).

3.4 | In vivo photothermal treatments

Encouraged by the selective delivery of exosomes to tumour areas we decided to evaluate the potential use of exosomes-gold nanoparticle hybrids as a vector of hyperthermia therapy in both in vivo tumoural models. To this end, 1.71×10^{10} particles of PEG-HGNs-sEVs^{hpMSCs} were administered in the tail vein of the animals. Mice in both tumour models were divided as follows: group 1 did not receive neither sEVs nor laser irradiation; mice of group 2 were irradiated with a NIR laser without administering sEVs; group 3 was treated with sEVs but without NIR laser application; and finally group 4 received both sEVs and irradiation with a NIR laser.

Mice with xenograft or multinodular models implanted were irradiated after 48 h and 72 h of the administration of the sEVs, respectively. These time points were chosen according to biodistribution results, in which the amount of PEG-HGNs-sEVs^{hpMSCs} was maximum in order to guarantee the best phototherapeutic effect. In the group of animals treated with the laser, the irradiation was applied always under sterile conditions and during 5 min at 2 and 1,5 W for the xenograft tumour and for the multinodular peritoneal cancerous areas, respectively. In the case of the multinodular tumour, an incision in the skin and in the peritoneum close to the pancreatic area was performed with a microscissor to introduce the 500 μm diameter laser diffusor in the peritoneum next to the pancreas, where most cancerous areas were located (see Figure S9D). After 1 week of the PEG-HGNs-sEVs^{hpMSCs} administration, a second injection of sEVs and a second irradiation (under the same conditions of the first one) were carried out. The evolution of the tumour size was measured by a caliper (in the xenograft model) and monitoring bioluminescence intensity with IVIS (for the multinodular model).

3.4.1 | Xenograft model

Tumour development in xenograft models was followed until they reached the ethically allowed size by the local committee. As Figures 5(a) and (b) indicate, tumour size for animals of the three control groups increased progressively over time. In contrast, the tumour of animals treated with PEG-HGNs-sEVs^{hpMSCs} and irradiated with the laser stopped growing after the first laser irradiation and decreased significantly after the second. After 27 days (the end of the experiment) the tumours in the group treated with sEVs and irradiated with NIR laser reduced strongly and almost disappeared, while they continued to grow in the control groups. These results show that sEVs not only deliver efficiently PEG-HGNs to the tumours but also that the particles preserve their photothermal properties in the process of encapsulation. In Figure 5(c), containing photographs of xenograft tumours from the first to the experimental end point, the evolution of the xenograft tumours in sEVs treated mice after the irradiation with the laser can be observed.

Figure S10 includes images of the experimental sequence of the irradiation procedure performed in both tumour models. In the case of the xenograft model, it is possible to observe how immediately after the application of the NIR laser, an inflammation and red areas appeared due to liquid infiltration and the vasodilatation after the burn produced by the temperature increase in the subcutaneous tumour. One week after the treatment, the wound was well recovered and healed by the formation of new skin tissue while tumour size was deeply reduced compared to the control group. During the second irradiation, tumours were mainly irradiated in the surroundings of the burn aiming for the complete elimination of any remaining growing tumoral cells. This could be done thanks to the nature of the xenograft model, where the tumoral mass is exposed. In contrast, regarding the multinodular model (bottom panel), the multiple cancerous areas could not be irradiated externally since they were located attached to the peritoneum or integrated in the pancreas. Thus, a small incision was performed to introduce the laser fibre in the mice' peritoneum to irradiate the tumoral regions. After 1 week, wounds were healed and the second sEVs administration and irradiation could be carried out.

Given the special conditions of the intraperitoneal irradiation for the multinodular model, the parameters (time, power and temperature) of laser application in the multinodular model were optimized before performing the experiments. In Figure S11 the evolution of the temperature in the liver, pancreas and spleen of sacrificed animals is shown when they were irradiated at different laser powers (1.5; 2 and 2.5 W). A power of 1.5 W and irradiation time of 5 min was chosen for the in vivo intraperitoneal irradiation experiments.

The temperature achieved during the irradiation of the xenograft and the multinodular tumours when they were irradiated after the PEG-HGNs-sEVs^{hpMSCs} administration is included in Figure S12. The histopathological analysis of the skin of animals containing the xenograft model indicate that in the case of the skin from mice treated with laser without sEVs, they presented an intact epidermis and dermis over the tumour mass. On the contrary, in the case of mice treated with the laser and the sEVs containing the nanoparticles, the skin above the tumour and the tumour itself were coagulated as a result of overheating (Figure S13).

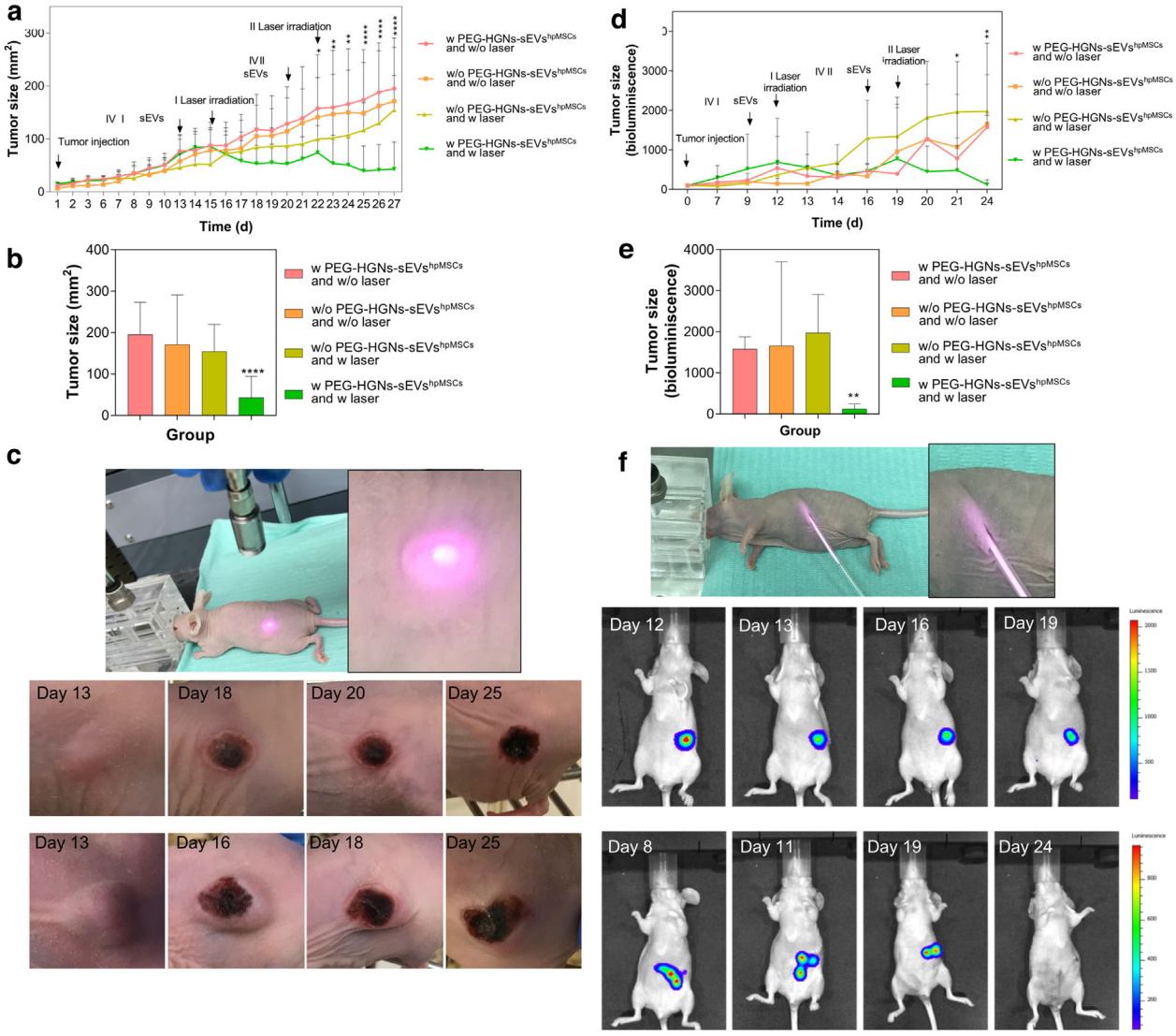

FIGURE 5 Photothermal therapy on xenograft (left) and multinodular (right) tumours after IV injection of PEG-HGNs-sEVs^{hpMSCs}. (a) Tumour size evolution for the three control groups and the treated one. The arrows indicate the implantation of the tumour, and the times for the two IV administrations of sEVs and the corresponding laser irradiations. (b) Tumour size of animal groups with the xenograft model at the end of the experiment (expressed in mm (Jhawar et al., 2017)) (c) Photographs of xenograft tumours from the first to the experimental end point. (d) Multinodular model tumour size evolution followed by quantification of the bioluminescence intensity of photons emitted from pancreatic tumoral. (e) Tumour size of animal groups in the multinodular model at the end of the experiment (indicated by bioluminescence intensity) (f) Representative IVIS images obtained during the course of the experiment. $^{*}p < 0.05$; $^{**}p < 0.01$; $^{****}p < 0.00001$

3.4.2 | Multinodular model

In this case, the evolution of the tumour was analysed by monitoring the bioluminescence of tumour cells by IVIS. As expected, the expression of luciferase was detected in the pancreatic region and, although it does not give an exact measurement of tumour size, its evolution serves the purpose of quantifying the relative variations of the number of tumoral cells. Figure 5(d) shows that, while luciferase expression increased during the 17 days of experiment on the control groups, it showed a pronounced decrease over time when the treatment was applied on the treated group. As in the xenograft model, the differences in the response of the multiple cancerous nodules between different groups became more pronounced after the second round of treatments. The bioluminescence intensity of the pancreas cancerous areas at the end of the experiments in the four groups given in Figure 5(e), and the snapshots of Figure 5(f) evidence the effectiveness of the NIR laser applications combined with the exosome-HGNs hybrid vectors with nearly complete disappearance of tumour cell luminescence after the two sEVs administrations and the corresponding irradiations with the NIR laser.

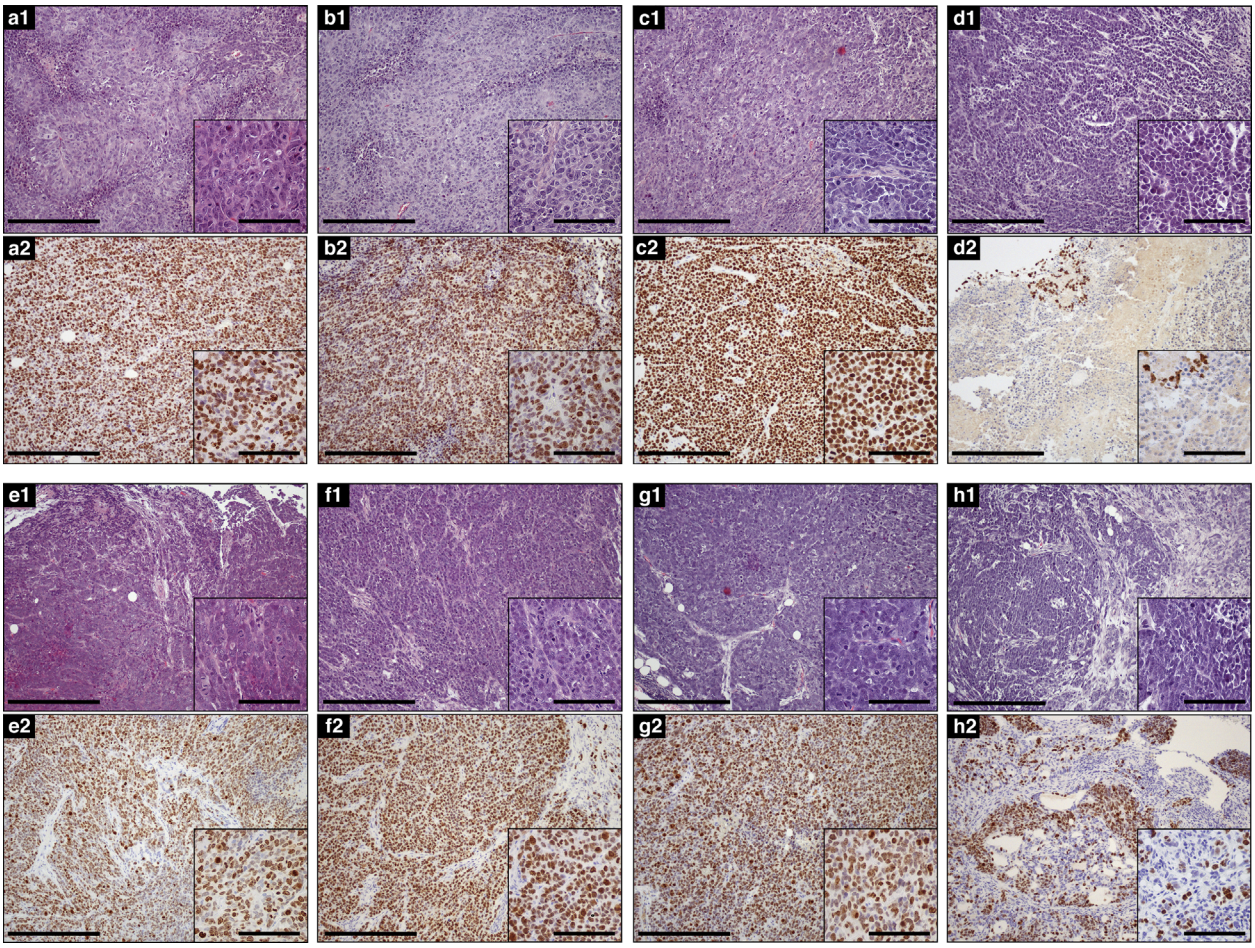

FIGURE 6 Histopathological analysis of tumours in xenograft (a–d) or multinodular models (e–h). Columns correspond to groups; AandE: Control 1. w/o laser and w/o PEG-HGNs-sEVs^{hpMSCs}; B&F: Control 2. w laser and w/o PEG-HGNs-sEVs^{hpMSCs}; C&G: Control 3. w/o laser and w PEG-HGNs-sEVs^{hpMSCs}; D&H: w PEG-HGNs-sEVs^{hpMSCs} and w laser. A1-H1: Hematoxylin-Eosin (HE) A2-H2: Ki-67 immunohistochemical staining. A1-C1/E1-G1: Tumour cells growing in a solid pattern and showing cellular characteristics of malignancy, such as atypical mitosis. Cytoplasm and nuclei limits are readily distinguished (insets). D1-H1: Tumour cells after treatment. Cells have lost their definition, becoming an almost amorphous basophilic mass where it is difficult to discern the border between nucleus and cytoplasm (insets). A2-C2/E2-G2: Almost all tumour cells are positive for Ki-67 staining. D2-H2: Ki-67 staining is almost abrogated in both tumour models, with the exception of a few cells. Notably, masses in the multinodular model located after treatment were few. Bars 300 μm, Inset bars 100 μm

3.4.3 | Histopathological analysis

To verify the efficacy of the antitumoral treatment mediated by optical hyperthermia, a histopathological analysis comparing control groups with the treated group was carried out by H-E and Ki-67 stainings. Ki-67 is a nuclear antigen employed as biomarker for cell proliferation. Ki-67 expression in tumours is strictly associated with cell proliferation and it has been correlated with an increased growth rate and aggressiveness of cancer cells (Maeyama et al., 2021). This protein has a crucial role in cell cycle regulation: it is absent in cells that are not in a replicating phase, reaching maximum expression levels during cell mitosis. Histopathologic analysis indicated that in all groups in both tumoral models, HE staining demonstrated a massive growth of tumour cells usually adopting a solid pattern, cells showing histopathologic features of malignancy such as cellular anaplasia, nuclear enlargement high mitotic index and atypical mitosis (Figure 6a1–6d1 and 6e1–6h1 and insets). Tumour cells in the three control groups of both tumoral models showed a fine definition of basophilic nucleus together with eosinophilic cytoplasm (Figures 6a1–6c1 and 6e1–6g1 and insets). However, in the treated group this characteristic definition was totally abrogated, tumour cells becoming an amorphous basophilic mass where the nucleus was difficult to distinguish (Figures 6d1 and 6h1, and insets). This morphology is most likely due to coagulation of proteins, nucleic acids and other cellular components following overheating induced by the laser treatment in sEVs-containing tumour cells. Analysis performed by Ki-67 indicated that almost all tumour cells were strongly positive, thus indicating an active proliferative status corresponding to cells that are in continuous division (Figures 6a2–6c2 and 6e2–6g2 and insets). However, sEVs-treated tumour cells of the xenograft model lost almost completely this positive signal, with sporadic groups of a few positive cells remaining, normally located at the edges of the section

TABLE 1 Percentage of Ki-67 positive tumour cells in both, xenograft or multinodular tumour model

	Group	% of positive staining Ki-67 cells
Xenograft model	Control 1) w/o laser and w/o PEG-HGNs-sEVs^{hpMSCs}	90.9 ± 14.4
	Control 2) w laser and w/o PEG-HGNs-sEVs^{hpMSCs}	93.6 ± 9.3
	Control 3) w/o laser and w PEG-HGNs-sEVs^{hpMSCs}	96.3 ± 5.9
	w PEG-HGNs-sEVs^{hpMSCs} and w laser	**1.4 ± 2.2**
Multinodular model	Control 1) w/o laser and w/o PEG-HGNs-sEVs^{hpMSCs}	86.2 ± 17.5
	Control 2) w laser and w/o PEG-HGNs-sEVs^{hpMSCs}	65.3 ± 28
	Control 3) w/o laser and w PEG-HGNs-sEVs^{hpMSCs}	66.9 ± 22.8
	w PEG-HGNs-sEVs^{hpMSCs} and w laser	**5.9 ± 5.4**

Protein expression was studied in all groups by counting positive and negative cells in three acquisition images from all animals using ImageJ software. Data was expressed as the percentage of positive cells.

(Figure 6d2 and inset). A similar situation was observed in the sEVs-treated tumour cells of the multinodular model. In this case, most animals treated with the sEVs and with the laser did not contain tumour nodules. And, only few mice contained tumour nodules after the treatment. Ki-67 staining was mostly abrogated in the few masses that could be located at postmortem. The lost Ki-67 signal in the treated groups of both tumoral models agrees with massive protein coagulation and irreversible changes in Ki-67 protein tertiary structure, indicating loss of viability (Table 1).

On the contrary, the treatment group exhibited only 1.4% of positive Ki-67 stained cells. In the multinodular model, the three control groups ranged from 65 to 86% of cells positive for Ki-67, compared to a 5.9% for the treatment group.

4 | DISCUSSION

Selective delivery of sufficient therapeutic NPs to a growing tumour still remains a bottleneck in nanomedicine. As shown in recent reports (Wilhelm et al., 2016), in spite of many efforts decorating the surface of NPs with different targeting agents such as peptides, aptamers or antibodies the delivery efficiency remains stuck around 1%, not much higher than EPR-based delivery. Considering that, we have employed sEVs as alternative delivery agents to drive NPs to target sites. Because sEVs can be produced by almost all cell lines, different types of EVs can exhibit a broad range of behaviours on account of their content of biomolecules and physicochemical properties including membrane composition. The often reported specific tropisms, fingerprint characteristics and selective functions depend on these features. It is generallt thought that the cellular source for sEVs is responsible for the greater part of these characteristics and therefore the question arises of whether the specific results found for a given scenario and class of EVs hold only for the system investigated. Indeed, there are many options to choose from. In particular, the use of tumoral sEVs from the same cancer line is a clear area of interest,[24, 25] but concerns regarding their potential risk in giving rise to a faster tumor growth represent a serious issue that hinders their clinical use. EVs from other very interesting sources, such as those coming from dendritic cells[26] or more recently CAR-T cells,[27] have exciting properties that surely will give rise to specific applications. In this work we have used mesenchymal stem cell derived sEVs, widely considered as promising nanoparticle carriers in the fields of regenerative medicine, cell therapy and tissue engineering.[28,29,30] MSCs sEVs have been extensively tested in multiple studies[31,32] and are already being used in clinical trials as they are generally deemed safe carriers.[33] These factors prompted us to use MSC-derived sEVs as nanoparticle delivery vectors in this work. Our results show that for this particular case, they were succesful in enhancing nanoparticle delivery. However, further investigation with other animal models is needed to confirm the validity of this approach.

In this work for the first time, to the best of our knowledge we have compared EPR-based and sEVs-based delivery of HGNs for hyperthermia treatment. Our results show that the delivery of gold NPs to a xenograft tumour via sEVs isolated from mesenchymal stem cells was roughly quadrupled compared to the delivery of pegylated nanoparticles via EPR effect. More interestingly, the stem cell derived sEVs were also able to deliver the same hollow gold NPs to a disseminated multinodular model, again multiplying by four the amount of gold delivered to the tumoral areas, according to our biodistribution results that analysed the gold effectively delivered to different organs. This targeting advantage provided by stem cells sEVs may be attributed to their small size, hydrodynamic diameter and to their intact membranes, thanks to the natural biogenesis procedure used to harvest loaded sEVs. Compared to other encapsulation procedures, this preserves the recognition moieties integrins and selectins present on their membrane (Sancho-Albero et al., 2019). However, some publications have reported the accumulation of the extracellular vesicles derived from stem cells in lungs after 5 and 24 h of their administration (Gangadaran et al., 2018, Grange et al., 2014). In experiments injecting mesenchymal stem cells in vivo, it has been reported that they were initially distributed in the lungs, but after

72 h they were spread throughout the whole organism (Kidd et al., 2009). Apparently, our sEVs share some of these features from their parental cells (Sancho-Albero et al., 2019), leading to an initial accumulation of the PEG-HGNs-sEVs^{hpMSCs} in the lungs followed by a later dissemination in the organism. In the liver, a significant accumulation was also observed. Previous works have shown that fluorescently labelled extracellular vesicles accumulate mainly in the liver after intravenous administration (Institutet et al., 2015). In our case, high fluorescence levels were still observed after 1, 2, 3 and 7 days of their injection.

In summary, these results show that stem cells sEVs-based delivery is far superior to EPR effect when targeting tumours. This is not surprising since the uncertainty and heterogeneity regarding the effectiveness of the EPR effect has been widely noticed (Maeda, 2015). However, in this case we show that the effectiveness is strongly increased even in the case of multinodular dissemination, always a challenging scenario for delivery.

Although the majority of the gold still ended in the liver and spleen with both delivery methods, the sEVs-mediated accumulation of NPs in both tumoral models was high enough to produce a strong decrease of tumour size, leading to nearly complete eradication upon NIR laser irradiation at the time of maximum accumulation (between 48 and 72 h after injection). The immunohistopathological analysis (H&E and Ki-67 staining) corroborated the efficiency of the optical hyperthermia therapy, indicating a profound morphological change in treated tumour cells and a remarkable decrease of Ki-67 expression in the treatment group, that lead to total disappearance of tumour masses in some cases.

Taken together, when the natural biogenesis pathway is leveraged to obtain nanoparticle-loaded sEVs, a powerful hyperthermia-capable vector is obtained that combines the targeting capabilities of the intact sEVs membrane and the NIR-absorbing properties of the HGN load. In this study, the targeting properties of stem cell derived sEVs in combination with NPs have been evaluated. However, other type of EV sources might provide comparable or even superior characteristics, and could be potentially considered for being used as efficient delivery vehicles, as well. The successful results in the case of the multinodular model, that represents a disseminated tumour resembling a metastatic scenario, are especially promising and show the potential of stem cells derived- sEVs-nanoparticle hybrids in the field of cancer treatment by novel noninvasive strategies.

AUTHOR CONTRIBUTION

María Sancho-Albero prepared and characterized the materials, performed and planned the experiments, analysed the data and contributes to the manuscript writing. Miguel Encinas-Gimenez and Victor Sebastian performed part of the in vitro experiments and Victor Sebastian carried out electron microscopy characterization. Pilar Martin-Duque contributed to the in vivo experiments. Pilar Martin-Duque and Jesús Santamaría planned, coordinated and supervised the research, analysed the data, contributed to the manuscript witting and conceived the research. Estela Pérez and Lluís Luján carried out the histopathological analysis and contributed to manuscript writing. All authors checked the manuscript.

ACKNOWLEDGEMENTS

We gratefully acknowledge financial support from the ERC Advance Grant CADENCE (grant no- ERC-2016-ADG-762684). María Sancho-Albero thanks the Spanish Government for an FPU PhD research fellowship (reference 15/03419). Pilar Martin-Duque also thanks Instituto de Salud Carlos III (PI19/01007 and DTS21/00130) and V.S acknowledges Fundación Ramón Areces (XX concurso nacional-ciencias de la vida y la materia) and beca Leonardo a Investigadores y creadores culturales 2021 de la Fundación BBVA. We would like to thanks to the Scientific Services of the Aragon Institute of Health Sciences (IACS), specifically to the Microscopy and Imaging, Pathology and Animal Facilities Services and their specialist and the ICTS ELECMI (LMA-UNIZAR).

CONFLICT OF INTEREST

The authors declare no competing interests.

REFERENCES

Alhasan, A. H., Patel, P. C., Choi, C. H. J., & Mirkin, C. A. (2009). Exosome encased spherical nucleic acid gold nanoparticle conjugates as potent microRNA regulation agents. *Small 6*, 247–253.

Betzer, O., Perets, N., Angel, A., Motiei, M., Sadan, T., Yadid, G., Offen, D., & Popovtzer, R. (2017). In vivo neuroimaging of exosomes using gold nanoparticles. *ACS Nano 11*, 10883–10893.

Colombo, M., Raposo, G., & Théry, C. (2014). Biogenesis, secretion, and intercellular interactions of exosomes and other extracellular vesicles. *Annual Review of Cell and Developmental Biology 30*, 255–289.

Gangadaran, P., Hong, C. M., Oh, J. M., Rajendran, R. L., Kalimuthu, S., Son, S. H., Gopal, A., Zhu, L., Baek, S. H., Jeong, S. Y., Lee, S. W., Lee, J., & Ahn, B. C. (2018). In vivo non-invasive imaging of derived from red blood cells in mice. *Front P 9*, 1–13.

Grange, C., Tapparo, M., Bruno, S., Chatterjee, D., Quesenberry, P. J., Tetta, C., & Camussi, G. (2014). Biodistribution of mesenchymal stem cell-derived extracellular vesicles in a model of acute kidney injury monitored by optical imaging. *International Journal of Molecular Medicine 33*, 1055–1063.

Hood, J. L., Scott, M. J., & Wickline, S. A. (2014). Maximizing exosome colloidal stability following electroporation. *Analytical Biochemistry 448*, 41–49.

Hu, L., Wickline, S. A., & Hood, J. L. (2015). Magnetic resonance imaging of melanoma exosomes in lymph nodes. *Magnetic Resonance in Medicine 74*, 266–271.

IARC- International Agency for Research on Cancer. (2020). Pieejams: https://www.iarc.fr

Institutet, K., Nordin, J., Institutet, K., & Loughlin, A. O. (2015). Extracellular vesicle in vivo biodistribution is determined by cell source, route of administration and targeting. *Journal of Extracellular Vesicles 4*, 26316.

Jhawar, S. R., Thandoni, A., Bommareddy, P. K., Hassan, S., Kohlhapp, F. J., Goyal, S., Schenkel, J. M., Silk, A. W., & Zloza, A. (2017). Oncolytic viruses—Natural and genetically engineered cancer immunotherapies. *Frontiers in Oncology 7*, 202.

Kahlert, C., & Kalluri, R. (2013). Exosomes in tumor microenvironment influence cancer progression and metastasis. *Journal of Molecular Medicine 91*, 431–437.

Khongkow, M., Yata, T., & Boonrungsiman, S. (2019). Surface modification of gold nanoparticles with neuron-targeted exosome for enhanced blood – brain barrier penetration. *Science Reports 9*, 1–9.

Kidd, S., Spaeth, E., Dembinski, J. L., Dietrich, M., Watson, K., Klopp, A., Battula, V. L., Weil, M., Andreeff, M., & Marini, F. C. (2009). Direct evidence of mesenchymal stem cell tropism for tumor and wounding microenvironments using in vivo bioluminescence imaging. *Stem Cells 27*, 2614–2623.

Lachenal, G., Pernet-Gallay, K., Chivet, M., Hemming, F. J., Belly, A., Bodon, G., Blot, B., Haase, G., Goldberg, Y., & Sadoul, R. (2011). Release of exosomes from differentiated neurons and its regulation by synaptic glutamatergic activity. *Molecular and Cellular Neuroscience 46*, 409–418.

Lara, P., Palma-Florez, S., Salas-Huenuleo, E., Polakovicova, I., Guerrero, S., Lobos-Gonzalez, L., Campos, A., Muñoz, L., Jorquera-Cordero, C., Varas-Godoy, M., Cancino, J., Arias, E., Villegas, J., Cruz, L. J., Albericio, F., Araya, E., Corvalan, A. H., Quest, A. F. G., & Kogan, M. J. (2020). Gold nanoparticle based double - labeling of melanoma extracellular vesicles to determine the specificity of uptake by cells and preferential accumulation in small metastatic lung tumors. *Journal of Nanobiotechnology 18*, 1–17.

Maeda, H. (2015). Toward a full understanding of the EPR effect in primary and metastatic tumors as well as issues related to its heterogeneity. *Advanced Drug Delivery Reviews 91*, 3–6.

Maeyama, M., Tanaka, K., Nishihara, M., Irino, Y., Shinohara, M., Nagashima, H., Tanaka, H., Nakamizo, S., Hashiguchi, M., Fujita, Y., Kohta, M., Kohmura, E., & Sasayama, T. (2021). Metabolic changes and anti-tumor effects of a ketogenic diet combined with anti-angiogenic therapy in a glioblastoma mouse model. *Science Reports 11*, 79.

Prat, A., & Baselga, J. (2008). The role of hormonal therapy in the management of hormonal-receptor-positive breast cancer with co-expression of HER2. *Nature Clinical Practice Oncology 5*, 531–542.

Rastinehad, A. R., Anastos, H., Wajswol, E., Winoker, J. S., Sfakianos, J. P., Doppalapudi, S. K., Carrick, M. R., Knauer, C. J., Taouli, B., Lewis, S. C., Tewari, A. K., Schwartz, J. A., Canfield, S. E., George, A. K., West, J. L., & Halas, N. J. (2019). Gold nanoshell-localized photothermal ablation of prostate tumors in a clinical pilot device study. *Pnas 116*, 18590LP–18596.

Roma-Rodrigues, C., Pereira, F., de Matos, A. P. A., Fernandes, M., Baptista, P. V., & Fernandes, A. R. (2017). Smuggling gold nanoparticles across cell types – A new role for exosomes in gene silencing. *Nanomedicine Nanotechnology, Biological Medicine 13*, 1389–1398.

Sancho-Albero, M., Encabo-Berzosa, M. D. M., Beltrán-Visiedo, M., Fernández-Messina, L., Sebastián, V., Sánchez-Madrid, F., Arruebo, M., Santamaría, J., & Martín-Duque, P. (2019). Efficient encapsulation of theranostic nanoparticles in cell-derived exosomes: Leveraging the exosomal biogenesis pathway to obtain hollow gold nanoparticle-hybrids. *Nanoscale 11*, 18825–18836.

Sancho-Albero, M., Navascués, N., Mendoza, G., Sebastián, V., & Arruebo, M. (2019). Exosome origin determines cell targeting and the transfer of therapeutic nanoparticles towards target cells. *Journal of Nanobiotechnology 17*, 1–13.

Sancho-Albero, M., Rubio-Ruiz, B., Pérez-López, A. M., Sebastián, V., Martín-Duque, P., Arruebo, M., Santamaría, J., & Unciti-Broceta, A. (2019). Cancer-derived exosomes loaded with ultrathin palladium nanosheets for targeted bioorthogonal catalysis. *Nature Catalysis 2*, 864–872.

Shahabipour, F., Barati, N., Johnston, T. P., Derosa, G., Maffioli, P., & Sahebkar, A. (2017). Exosomes: Nanoparticulate tools for RNA interference and drug delivery. *Journal of Cellular Physiology 232*, 1660–1668.

Sharma, S. K., Shrivastava, N., Rossi, F., Tung, L. D., & Thanh, N. T. K. (2019). Nanoparticles-based magnetic and photo induced hyperthermia for cancer treatment. *Nano Today 29*, 100795.

Wilhelm, S., Tavares, A. J., Dai, Q., Ohta, S., Audet, J., Dvorak, H. F., & Chan, W. C. W. (2016). Analysis of nanoparticle delivery to tumours. *Nature Reviews Materials 1*, 1–12.

Yong, T., Zhang, X., Bie, N., Zhang, H., Zhang, X., Li, F., Hakeem, A., Hu, J., Gan, L., Santos, H. A., & Yang, X. (2019). Tumor exosome-based nanoparticles are efficient drug carriers for chemotherapy. *Nature Communication 10*, 3838.

Zhuang, M., Chen, X., Du, D., Shi, J., Deng, M., Long, Q., Yin, X., Wang, Y., & Rao, L. (2020). SPION decorated exosome delivery of TNF-α to cancer cell membranes through magnetism. *Nanoscale 12*, 173–188.

SUPPORTING INFORMATION

Additional supporting information may be found in the online version of the article at the publisher's website.

How to cite this article: Sancho-Albero, M., Encinas-Giménez, M., Sebastián, V., Pérez, E., Luján, L., Santamaría, J., & Martin-Duque, P. (2022). Transfer of photothermal nanoparticles using stem cell derived small extracellular vesicles for in vivo treatment of primary and multinodular tumours. *Journal of Extracellular Vesicles*, *11,* e12193. https://doi.org/10.1002/jev2.12193